

Coherent Vibrational Quantum Beats as a Probe of Langmuir–Blodgett Monolayers

Andrey N. Bordenyuk, Himali Jayathilake, and Alexander V. Benderskii*

Department of Chemistry, Wayne State University, Detroit, Michigan 48202

Received: March 30, 2005; In Final Form: June 13, 2005

We combine frequency- and femtosecond time-domain measurements of vibrational coherences for spectroscopic characterization of surface monolayer films, utilizing 3-wave mixing as the surface-selective technique. Frequency-domain spectra in the CH-stretch region are obtained by infrared + visible sum frequency generation (SFG). Time-domain coherences are measured using SFG free induction decay (SFG-FID), where a 75 fs IR pulse excites several vibrational modes and a delayed 40 fs visible pulse probes the oscillating surface polarization. A unified framework based on optical Bloch equations is used to simultaneously analyze the time- and frequency-domain data. We compare molecular organization of monolayers in different two-dimensional phases. Highly ordered films transferred at high surface pressure are dominated by two transitions in the frequency domain, CH₃ symmetric stretch (2875 cm⁻¹) and CH₃–Fermi resonance with bend overtone (2935 cm⁻¹), and a coherent quantum beat in the time-domain at the difference frequency (~540 fs period). At lower surface pressure, relative amplitudes change and additional transitions emerge (CH₃ asymmetric stretch and CH₂ modes), indicating changes in molecular orientation and onset of disorder. Information redundancy in the combined frequency- and time-domain data allows more accurate determination of the spectral parameters than purely frequency- or time-domain techniques.

1. Introduction

Time-resolved coherent vibrational spectroscopy holds great promise as a noninvasive technique capable of providing information about molecular structure and dynamics on the time scale relevant to elementary chemical and biological processes.^{1,2} The wealth of information regarding chemical structure contained in the fingerprint mid-IR region of the spectrum can be augmented by measurements of vibrational coherences to characterize, e.g., coupling between modes.^{2,3} A great deal of activity has been recently directed toward the development of coherent vibrational techniques for the condensed phases such as bulk liquids.^{4–10}

Surfaces and interfaces present a class of systems that are in many instances as important as the bulk condensed phases. In contrast to the burgeoning field of bulk condensed-phase time-domain vibrational spectroscopy, relatively few studies of femtosecond dynamics of vibrational coherences on surfaces have been reported. The idea of following vibrational dephasing on surfaces using a femtosecond IR pulse excitation and a visible pulse up-conversion in a surface-selective 3-wave mixing scheme was first demonstrated in 1991 with picosecond¹¹ and sub-picosecond resolution.¹² Decay of the vibrational coherence of a single mode on a solid surface under high vacuum (e.g., CO on Cu(111)¹² or Si–H on Si(111)¹¹) was monitored and found to be in agreement with the spectral width measured in the frequency domain. More recently, this sum frequency generation free induction decay (SFG-FID) technique was applied to similar systems^{13–17} and extended to Langmuir–Blodgett monolayers¹⁸ and to a liquid/solid (acetonitrile/gold) interface.¹⁹

In this paper, we combine the frequency-domain SFG spectroscopy and the time-domain SFG-FID technique for characterization of more complex molecular surfaces under

ambient conditions. Langmuir–Blodgett (LB) transfer is receiving increased attention as a method of manufacturing molecularly ordered monolayer materials for a variety of applications. In particular, they are of current interest for preparation of organic and molecular electronic materials and devices^{20–25} and organic ferroelectrics for polar switching memory elements.^{26,27} In the majority of these applications, molecular order plays crucial role in determining the performance characteristics. Nevertheless, many details of the molecular organization remain unclear, such as molecular orientation and conformational state corresponding to different two-dimensional 2D phases and mesophases of the LB monolayers.

The Langmuir–Blodgett monolayers of heptadecanoic acid (HDA, C₁₇ fatty acid) were chosen as a model system because the structure and 2D phases of the precursor Langmuir films have been extensively characterized by various techniques such as tensiometry, X-ray diffraction, and Brewster angle microscopy (BAM).^{28–32} Figure 1 shows the pressure–area per molecule isotherm of HDA on water subphase at 21 °C measured in this study, also indicating the 2D phases and related mesophases from X-ray and BAM studies.^{30–32} In particular, X-ray diffraction studies show that monolayers in each of these phases are characterized by different hexagonal unit cells. X-ray studies also yield information about alkyl chain tilt and twist angles, as well as the magnitude of the unit cell distortion due to chain tilt and backbone plane ordering.³⁰ The liquid expanded (LE) phase, isotropic with tilted molecules, corresponds to area 30–40 Å² per molecule. The liquid condensed (LC) phase has two mesophases: the lower pressure mesophase L_{2d} (upper bound pressure ~16 mN/m) with a collective tilt of the alkane chains toward the nearest neighbor (NN), and the higher pressure mesophase O_v (surface pressure range 16–26 mN/m) with alkane chains tilted toward the next-nearest neighbor (NNN). The transition L_{2d}–O_v occurs without singularity on the pressure–area isotherm. The superliquid phase (LS), an untilted

* Corresponding author. E-mail: alex@chem.wayne.edu

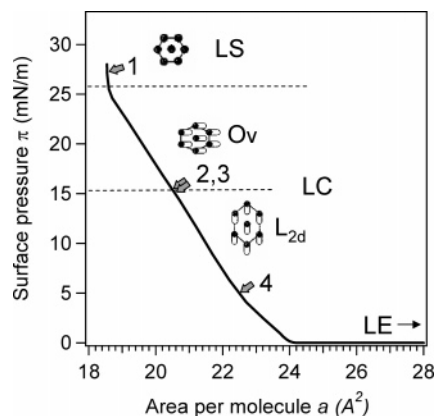


Figure 1. Pressure–area (π – a) isotherm of heptadecanoic acid on water subphase measured at 21 °C. The 2D phases and mesophases, based on literature reports, are illustrated. Arrows indicate pressures at which the investigated samples 1–4 were prepared.

phase without regular twist angle of alkane chains within the unit cell, corresponds to pressure range 26–40 mN/m.³¹

In the present paper we develop an approach to structural (and dynamical) characterization of LB monolayer films by combining time- and frequency-domain SFG spectroscopy in a unified framework which allows simultaneous analysis to utilize the information redundancy in the time- and frequency-resolved data. Two or more vibrational modes of the LB monolayer surface are simultaneously excited by a femtosecond IR pulse, and the created time-dependent vibrational coherences are monitored using surface-selective SFG up-conversion. The time-domain SFG-FID measurements are complemented by the frequency-domain SFG spectroscopy. Since both measurements involve a single (vibrational) resonant interaction, the combined time- and frequency-domain data sets contain redundant information on the one-dimensional molecular response function. This redundancy helps combat measurement noise and achieve more accurate determination of the molecular response function parameters. The approach may be useful for complex molecular systems characterized by congested frequency-domain spectra with overlapping bands, such as LB monolayers in various 2D phases. We parametrize the response function for the LB monolayers using a model based on optical Bloch equations, which represents the monolayer as a collection of uncoupled vibrations with exponential relaxation. The extracted parameters may be interpreted in terms of the molecular orientation and conformation in the different 2D phases and mesophases of the LB monolayers transferred onto the hydrophilic substrate under different surface pressures. The molecular-level detail provided by the combined time- and frequency-domain SFG spectroscopy may thus prove complementary to surface characterization techniques such as surface tensiometry, X-ray diffraction, and Brewster angle microscopy.

2. Experimental Methods

2.1. Sample Preparation. Monolayers of heptadecanoic acid (HDA) were prepared by standard Langmuir–Blodgett transfer onto IR-grade fused silica substrates. The films were prepared at surface pressure 30 mN/m (sample 1), 15 mN/m (samples 2 and 3), and 5 mN/m (sample 4), representing different 2D phase and mesophases (Figure 1). Briefly, 60 μ L of 0.5 mg/mL solutions of HDA (Sigma, >98%) in chloroform helper solvent (Fisher Scientific, spectral analyzed grade) were spread on the water subphase in a LB Minitrough (KSV Instruments) using a microsyringe. A deionized water bath (Julabo F12) was used

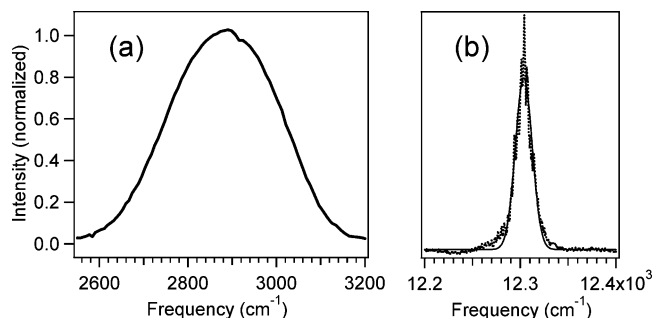


Figure 2. Spectra of broad-band IR (a) and narrow-band visible (b) pulses used in the frequency-domain broad-band SFG measurement.

for the sample preparation. After spreading the surfactant, it was kept for 30 min before compression to allow evaporation of chloroform and equilibration of a homogeneous HDA film on the water surface. The film was compressed by the computerized LB trough with the compression rate of 20 mm/min for surface pressure 5 and 15 mN/m and 1 mm/min to achieve pressure 30 mN/m. After obtaining the target pressure, the film was allowed to equilibrate for 40 min for pressure stabilization and relaxation of HDA monolayers³³ before transfer. The films were vertically transferred onto round IR-grade quartz windows (1 in. diameter, 1 mm thick) while keeping constant surface pressure. An elevation rate of 1 mm/min was used for pressure 5 and 15 mN/m and 0.1 mm/min for pressure 30 mN/m. All experiments (surface tension and SFG spectroscopy) were conducted at room temperature, 21.0 ± 0.5 °C.

2.2. SFG Setup. Our experimental setup, capable of both frequency- and time-domain sum frequency generation (SFG) spectroscopy, is based on a high power amplified femtosecond Ti–sapphire laser system (Spectra Physics Spitfire sub-50 fs HP). 50% of the 2 mJ fundamental output pulse (800 nm, fwhm 40 fs measured using a home-built noncollinear single-shot autocorrelator) is used to pump an optical parametric amplifier (OPA) followed by the signal–idler difference frequency mixing (DFM) in a 0.5 mm thick AgGaS₂ crystal, producing 75 fs IR pulses (measured as described below) centered at 2900 cm^{-1} . Spectra of the IR pulses (Figure 2) were measured using an IR grating (blazed at 5 μm) in the monochromator and a liquid nitrogen (LN2) cooled MCT detector (IR Associates). The other half of the fundamental output was used for the visible beam for SFG as described below.

The IR and visible beams were spatially and temporally overlapped at the horizontal sample surface. The incidence angle for both beams is 65° from surface normal. To minimize the laser beam impact on the sample, we use large beam spot sizes at the surface, ~ 250 μm for IR and ~ 400 μm for visible. Polarization of the visible beam is controlled by using a zero-order half-wave plate, while the IR beam polarization can be made either horizontal or vertical by using a periscope before the sample. The laser power at the sample is 1–2 $\mu\text{J}/\text{pulse}$ for IR and up to 100 $\mu\text{J}/\text{pulse}$ for the visible. We note that the visible beam is nonresonant and does not cause any damage in the sample, which was verified by checking that the SFG signal intensity from the illuminated spot of the sample stays within 1% of its original value over the course of the experiment (several hours). The SFG signal reflected from the sample surface was recollimated, spatially and frequency filtered, passed through a 300 mm monochromator (Acton Spectra-Pro 300i), and detected using a LN2-cooled CCD (Princeton Instruments Spec-10:100B, 100×1340 pixels). The polarization combination used in these experiments is SSP (SFG–vis-IR), which was

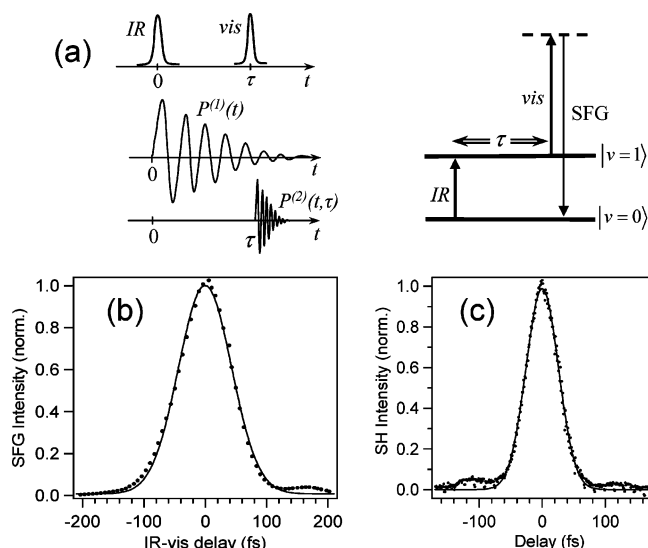


Figure 3. (a) Pulse sequence and level diagram of the SFG free induction decay (SFG-FID) time-domain 3-wave mixing. (b) SFG cross-correlation of the IR and visible pulses used in the time-domain SFG-FID. Thin line shows Gaussian fit, fwhm = 88.5 fs. (c) Autocorrelation of the visible pulse. Thin line shows Gaussian fit, fwhm = 41.5 fs.

found to produce the largest SFG signal for the LB samples. The signals were averaged over many laser shots ($\sim 10^5$ – 10^6) by using the CCD as the integrator. Typically, data collection time for the frequency-domain spectra was 15 min, and 3 min per each time-delay point in the time-domain measurements. The CCD image was processed using a LabView program to correct for the floating background (typically a few counts per hour) and cosmic X-rays. The background correction was performed by subtracting from the signal region of interest (e.g., horizontal strips 40–45), a nonilluminated region of the CCD of the same size (e.g., horizontal strips 80–85), at each acquisition point. Spikes due to the cosmic X-rays were eliminated using a differential discriminator program.

2.3. Frequency-Domain Measurements. For the frequency-domain spectroscopy, the broad-band SFG scheme^{34,35} was employed which uses spectrally broad IR and narrow visible pulses to obtain the spectrum by frequency-dispersing the SFG signal. A high-power deposited etalon (TecOptics) was used to narrow the spectrum of the visible pulse from 430 cm^{-1} of the Spitfire output to 18.3 cm^{-1} Gaussian fwhm centered at 809.3 nm (Figure 2). The SFG spectrum was obtained by the monochromator dispersing the signal onto the CCD, and vertical integration of the image. The spectral resolution of the BB-SFG is determined by the visible pulse bandwidth (Figure 2), since the monochromator disperses the SFG signal to $\sim 1.5\text{ cm}^{-1}$ per CCD pixel. After acquisition of the SFG spectra, 5-pixel binning of the CCD was performed to reduce noise without loss of spectral resolution. Deconvolution of the visible spectral width from the SFG spectra to obtain true line widths of the vibrational transitions is described in the Results section.

2.4. Time-Domain Measurements. The technique builds upon the purely time-domain method of SFG free induction decay (SFG-FID),^{11,12,18,36} in which a short IR pulse excites the vibrational coherence, creating an oscillating first-order polarization, and a delayed visible pulse probes its free induction decay (FID) by up-converting the oscillating surface polarization (Figure 3). For the time-domain SFG-FID measurements, short visible (40 fs) and IR (75 fs) pulses were used, with the time-delay controlled using a Newport VX-25 translation stage, with $0.1\text{ }\mu\text{m}$ (0.67 fs) accuracy. IR and visible beams are recombined

at the sample at a 2.5° angle to minimize broadening of the instrument response function due to the beam geometry. At this angle and the used beam sizes, the geometric broadening is estimated to be $\sim 25\text{ fs}$. The SFG-FID signal intensity is recorded as a function of the delay τ between the two pulses. For each IR-visible time delay the CCD image has been integrated over both coordinates, vertical and horizontal (frequency), to obtain intensity of FID. The results are plotted as a one-dimensional curve, total SFG-FID intensity vs time delay.

Instrument response function was measured by replacing the LB monolayer surface with a nonresonant substrate and recording the cross-correlation between the IR and visible pulses using the same process of surface SFG. The measured nearly Gaussian IR-vis cross-correlation function (fwhm = 88.5 fs) shown in Figure 3b thus represents the true instrument response of the SFG-FID measurement, including pulse widths at the sample and the geometric broadening. Three nonresonant substrate materials were used, Au, Ag, and CaF_2 , with CaF_2 typically giving slightly shorter cross-correlation (by ~ 2 – 3 fs), likely due to the pre-resonant excitation of the metal surface by the visible pulse. Gaussian fwhm of the IR pulses $\tau_{\text{IR}} = 75\text{ fs}$ was extracted by deconvolution from the IR-vis cross-correlation function using the visible pulse width (Figure 3c, Gaussian fwhm $\tau_{\text{vis}} = 41.5\text{ fs}$, measured using a home-built single-shot noncollinear autocorrelator) and the geometric factor. In addition, overall average linear chirp of the instrument response function was verified to be near zero by performing an SFG version of FROG measurement, where the IR pulse E-field at the surface is gated by the visible pulse field and the SFG signal is spectrally resolved.³⁷ We note that the pulses are not transform-limited and that the measured zero average chirp may result, e.g., from addition of the opposite sign chirps in the IR and visible pulses. The chirp may influence the FID curves at early time delays, e.g., for samples 3 and 4 (vide infra).

3. Results

The frequency-domain vibrational SFG spectra and the corresponding time-domain SFG-FID signals for Langmuir-Blodgett monolayers of heptadecanoic acid on fused silica are shown in Figures 4–7. Four samples are shown corresponding to different 2D phases indicated on the π - a isotherm in Figure 1. Sample 1 ($\pi = 30\text{ mN/m}$) is the superliquid phase LS. Samples 2, 3 ($\pi = 15\text{ mN/m}$), and 4 ($\pi = 5\text{ N/m}$) are in the liquid condensed phase LC, which contains several mesophases,³¹ with tentative assignments given in Table 1. For SFG spectra (Figures 4a–7a), the IR frequency is shown on the horizontal axis, calculated from the SFG frequency by subtracting the center frequency of the visible pulse, $\omega_{\text{IR}} = \omega_{\text{SFG}} - \omega_{\text{vis}}^0$. Figures 4b–7b show the SFG-FID measurements of the time-dependent vibrational coherence schematically depicted in Figure 3, where the total SFG intensity is plotted vs time delay between a short IR and a short visible pulse.

At high pressure qualitatively corresponding to more ordered films, samples 1 and 2, the frequency-domain SFG spectra (Figures 4a, 5a) are dominated by two transitions which can be assigned to the symmetric stretch of the terminal CH_3 group, $\nu(\text{r}^+) = 2875 \pm 1\text{ cm}^{-1}$, and CH_3 asymmetric bend overtone with intensity borrowed from r^+ by Fermi resonance, $\nu(\text{r}^+\text{FR}) = 2935 \pm 1\text{ cm}^{-1}$.³⁸ These frequencies are in good agreement with the reported values for similar films.^{39–43} The time-domain SFG-FID signals (Figures 4b, 5b) exhibit a pronounced quantum beat pattern at the difference frequency between the two coherently excited vibrational modes ($\Delta\nu \approx 60\text{ cm}^{-1}$ translates into $\sim 540\text{ fs}$ period). Semilog plots in the insets in

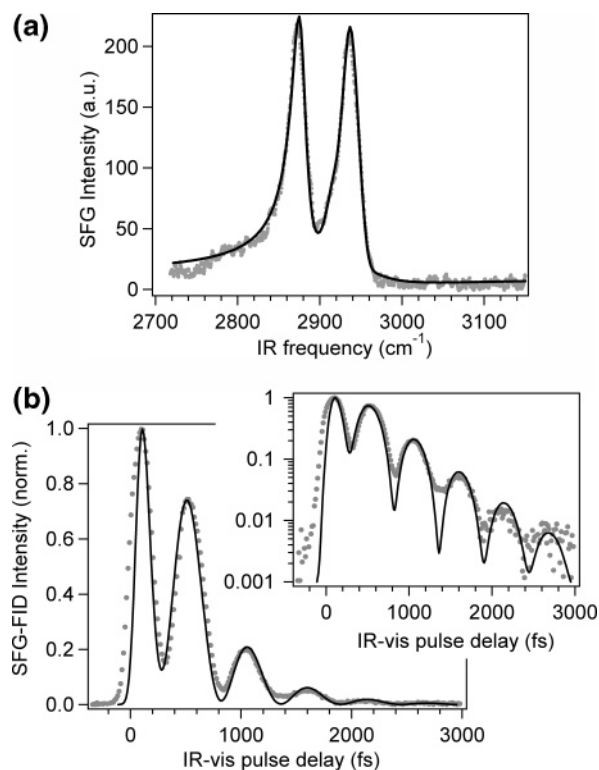


Figure 4. (a) Frequency-domain vibrational SFG spectrum of sample 1: Langmuir–Blodgett monolayer of heptadecanoic acid (HDA) transferred onto quartz substrate at surface pressure $\pi = 30$ mN/m. (b) Time-domain SFG-detected vibrational free induction decay (SFG–FID) for sample 1. Inset shows semilog plot of the same data. Solid lines in (a) and (b) show simultaneous fit using the model described in the Discussion section.

Figures 4b–6b show the feasibility of recording the beat pattern over almost 3 decades of the SFG–FID signal. Note that the time-domain instrument response function, $\text{fwhm} \approx 90$ fs, is considerably shorter than the observed coherent dynamics, allowing an almost purely time-domain measurement. Nevertheless, the pulse duration must be taken into account in the fitting of the SFG–FID data, as described in the next section.

At lower pressure, the SFG spectrum broadens (Sample 4, Figure 7a) due to weak shoulders appearing on the sides of the two main peaks. Simultaneous fitting of the spectra and the time-domain SFG–FID using the model based on optical Bloch equations described in the Discussion section indicates that the apparent broadening is caused not only by an increase in fwhm of the two main lines, r^+ and r^+_{FR} , but is mostly due to the emergence of additional lines in the SFG spectrum. The new bands can be assigned to CH_3 asymmetric stretch, $\nu(r^-) = 2956 \pm 5 \text{ cm}^{-1}$, and CH_2 symmetric and asymmetric stretches, $\nu(d^+) = 2850 \pm 5 \text{ cm}^{-1}$, $\nu(d^-) = 2915 \pm 5 \text{ cm}^{-1}$.^{38,44} The fast decay of the time-domain SFG–FID signal (Figure 7b) qualitatively indicates rapid dephasing of an ensemble of more than two coherently excited transitions with different frequencies.

The solid lines in Figures 4–7 show simultaneous fits of the SFG spectra and SFG–FID signal obtained within the model described in the next section. The molecular response function is parametrized by representing the LB monolayer as a collection of uncoupled two-level transitions ω_i with Lorentzian widths Γ_i (i.e., with time-domain dephasing time $\tau_i = 1/\Gamma_i$) and relative amplitude B_i . The parameters yielding the best fits for each sample are collected in Table 1. The true line widths for the vibrational transitions were obtained by deconvolution of the visible line width from the SFG spectra. The visible pulse

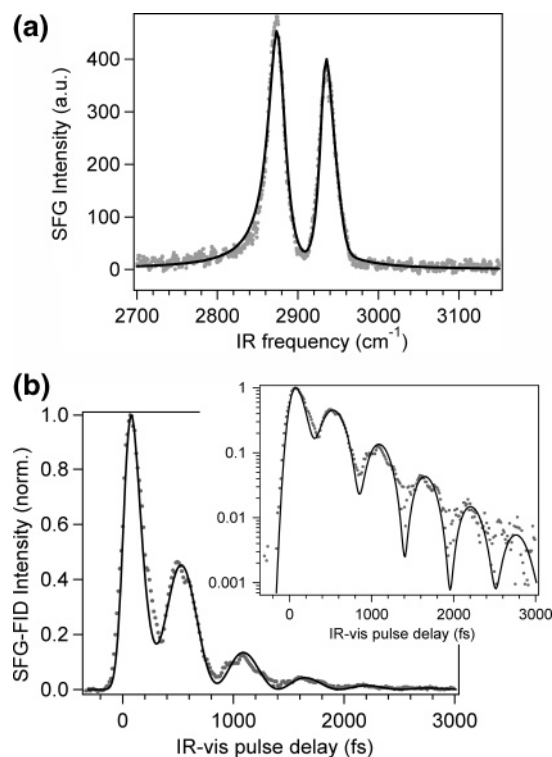


Figure 5. (a) Frequency-domain vibrational SFG spectrum of sample 2: LB monolayer of HDA, transfer pressure 15 mN/m. (b) Time-domain SFG–FID signal of Sample 2. Inset: Semilog plot of the same data. Solid lines in (a) and (b) show simultaneous fit using the model described in the Discussion section.

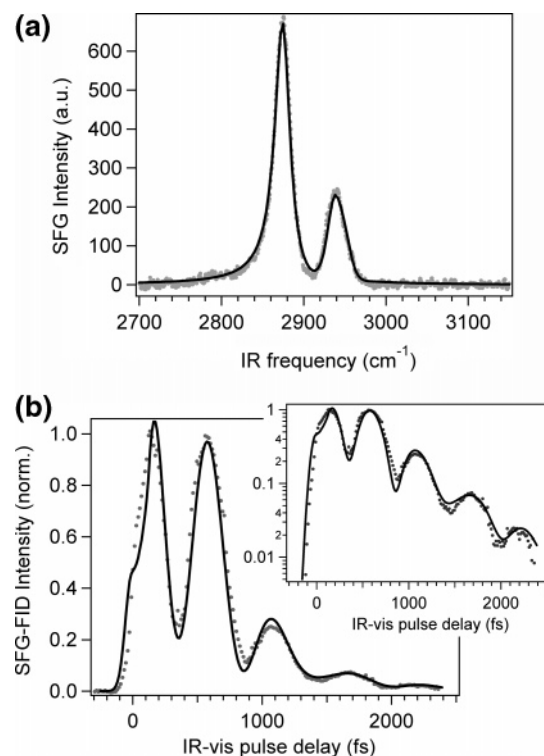


Figure 6. (a) Frequency-domain vibrational SFG spectrum of sample 3: LB monolayer of HDA, transfer pressure 15 mN/m (difference from sample 2 described in Results section). (b) Time-domain SFG–FID signal of sample 3. Inset: Semilog plot of the same data. Solid lines in (a) and (b) show simultaneous fit using the model described in the Discussion section.

spectrum is assumed to be Gaussian (Figure 2), while the vibrational resonances of the monolayer are treated as Lorent-

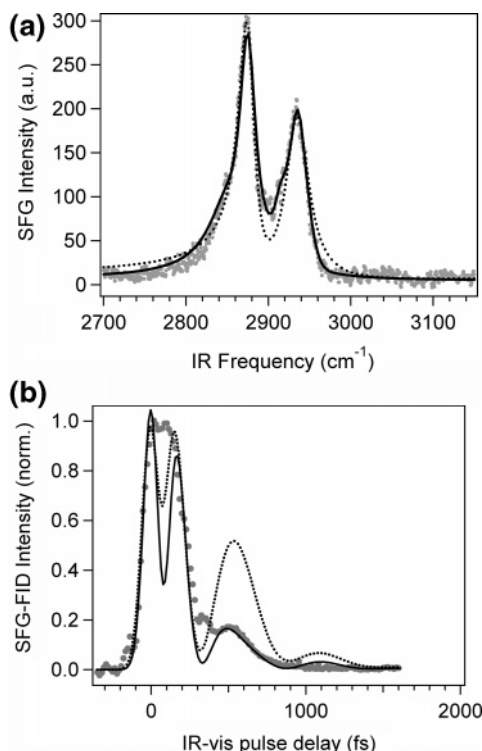


Figure 7. (a) Frequency-domain vibrational SFG spectrum of sample 4: LB monolayer of HDA, transfer pressure 5 mN/m. (b) Time-domain SFG-FID signal of sample 4. Solid lines in (a) and (b) show simultaneous fit using the model with five vibrational modes. Dotted lines: model fit using two vibrational modes (see Discussion section).

zians within the model. The convolution (the Voigt profile) was computed numerically for a fixed Gaussian (visible) and variable Lorentzian line width to yield a conversion curve from observed SFG line width to the true transition line width.

As seen in Figures 5 and 6 and Table 1, samples 2 and 3 transferred at nominally the same surface pressure $\pi = 15$ mN/m show significant differences both in their frequency-domain SFG spectra and in time-domain SFG-FID signals. We attribute this difference to the two different mesophases of the liquid condensed phase that exist above and below surface pressure of ~ 16 mN/m.^{30,31} Despite computer-controlled feedback, pressure overshoot is almost unavoidable during monolayer compression. During preparation of sample 3 (Figure 6), the

pressure after film compression exceeded the target value of 15 mN/m by about 0.5 mN/m, then relaxed monotonically to the target level without any oscillations. We also did not observe any pressure oscillation during the equilibration time for this sample. On the contrary, for sample 2 (Figure 5), the pressure after compression exceeded target value $\pi = 15$ mN/m by almost 2 mN/m, and relaxed to the target level manifesting significant oscillations, ~ 0.3 mN/m amplitude. The oscillations persisted over the 40 min equilibration time. We therefore tentatively attribute sample 3 to the lower-pressure L_{2d} mesophase of the liquid condensed phase with alkane chains tilted to nearest neighbor (LC-NN), while sample 2 may correspond to the higher-pressure O_v mesophase, with tilt toward next nearest neighbor (LC-NNN).³⁰

Interestingly, the SFG signals for samples 2 and 3 show azimuthal dependence with respect to the substrate withdrawal direction in the LB transfer procedure. The largest SFG signals are found when the incidence plane is along the direction of pull in the LB transfer process. Since the laser beam size is a few hundred μm , this indicates macroscopic alignment of molecules in the monolayer. Sample 1 ($\pi = 30$ mN/m), on the contrary, does not exhibit the azimuthal dependence, which may be indicative of the nearly vertical alignment of the alkyl chains in the 2D superliquid phase, in agreement with literature.^{30,31}

4. Calculation of Time- and Frequency-Domain SFG Signals

We begin by describing equations for calculating SFG signals which enable simultaneous fitting of the time- and frequency-domain data by properly accounting for the experimental pulse widths and spectral resolution. This simple model connects the information content of the frequency- and time-domain spectroscopic SFG data and allows us to take advantage of the information redundancy available from our experiment. The model treats the vibrational resonances of the LB monolayer as a collection of uncoupled two-level systems. The density matrix for the whole system is

$$\rho(t) = \sum_i B_i \rho^{(i)}(t) \quad (1)$$

where each sub-ensemble $\rho^{(i)}(t)$, contributing with weight B_i , represents a vibrational mode (i) observed in the frequency-domain spectrum and evolves according to optical Bloch

TABLE 1: Molecular Response Function Parameters Extracted from Simultaneous Fitting of the Frequency-Domain SFG Spectra and Time-Domain SFG-FID Measurements of Samples 1–4

#	π , mN/m	2D phase	no. of modes	vibr. mode ^a	ω_i (cm ⁻¹)	B_i (a.u.) ^b	Γ_i (cm ⁻¹)	A_{NR} ^b	φ_{NR} (rad)	η ^c
1	30	LS	3	r^+	2877 ± 1	1.0	4.5	-0.07	0.7	1.18
				r^+_{FR}	2937 ± 1	1.18	7.5			
				r^-	2956 ± 5	-0.15	5.5			
				d^-	2915 ± 5	0.08	5			
2	15	O_v	3	r^+	2875 ± 1	1.12	7.5	-0.03	0.8	0.86
				r^+_{FR}	2935 ± 1	0.96	4.0			
				r^-	2956 ± 5	-0.1	5.0			
				d^-	2915 ± 5	-0.32	4.5			
3	15	L_{2d}	3	r^+	2875 ± 1	1.32	5.0	-0.08	0.6	0.50
				r^+_{FR}	2934 ± 1	0.66	8.0			
				r^-	2956 ± 5	-0.32	4.5			
				d^-	2915 ± 5	0.32	28			
4	5	L_{2d}	5	r^+	2875 ± 2	1.01	7	-0.3	0.8	0.91
				r^+_{FR}	2934 ± 2	0.92	11			
				r^-	2956 ± 5	-0.42	24			
				d^-	2915 ± 5	0.32	28			
				d^+	2850 ± 5	0.34	21			

^a Vibrational mode assignments: r^+ – CH_3 symmetric stretch; r^+_{FR} – Fermi resonance between CH_3 symmetric stretch and bend overtone; r^- – CH_3 antisymmetric stretch; d^- – CH_2 antisymmetric stretch; d^+ – CH_2 symmetric stretch. ^b All amplitudes are in relative units normalized for the $B(r^+)$ value of the CH_3 SS for sample 1. ^c Amplitude ratio of the two main transitions, $\eta = B(r^+_{FR})/B(r^+)$.

equations^{45,46} with transition frequency ω_i and exponential total dephasing time constant $\tau_i = 1/\Gamma_i$ (i.e., Lorentzian spectral width Γ_i):

$$\dot{\rho}_{mn}^{(i)}(t) = (i\hbar)^{-1}([\hat{H}_0^{(i)}, \rho^{(i)}] + [\hat{H}_R^{(i)}, \rho^{(i)}]) = (-i\omega_{mn}^{(i)} - \Gamma_{mn}^{(i)})\rho_{mn}^{(i)}, m, n = 1, 2 \quad (2)$$

where

$$\hat{H}_0^{(i)} = \begin{bmatrix} \hbar\omega_i & 0 \\ 0 & 0 \end{bmatrix}$$

is the unperturbed Hamiltonian for a two-level system (i) and $\hat{H}_R^{(i)}$ phenomenologically represents relaxation.^{45–47}

After solving the Bloch equations (2) for individual subensembles and combining the solutions to compute the density matrix for the entire system, eq 1, we calculate the linear time-domain molecular response function (time-correlation function of the dipole moment operator) that characterizes evolution of the system after a single interaction with the vibrationally resonant IR field:⁴⁷

$$S(t) = A_{\text{NR}} e^{i\varphi_{\text{NR}}} \delta(t) - i\theta(t) \sum_i B_i \Gamma_i \exp(-i\omega_i t - \Gamma_i t) + [\text{c.c.}] \quad (3)$$

Here $\theta(t)$ is the Heaviside step function. Note that the time-domain response function is real. The first term accounts for the nonresonant (instantaneous) part of the response with amplitude A_{NR} and phase φ_{NR} with respect to the vibrationally resonant part of the response. The corresponding frequency-domain response function (at frequencies ω_{IR} near the vibrational resonances), connected to (3) by Fourier transform, reads

$$G(\omega_{\text{IR}}) = A_{\text{NR}} e^{i\varphi_{\text{NR}}} + \sum_i \frac{B_i \Gamma_i}{\omega_{\text{IR}} - \omega_i + i\Gamma_i} \quad (4)$$

The negative frequency components are omitted, hence the frequency-domain response function is complex-valued.

With the linear response functions parametrized by eqs 3 and 4 and the assumption that the visible field is nonresonant, calculation of the time- and frequency-domain SFG spectroscopic signals is straightforward.

In the time-domain SFG–FID, the IR pulse $E_{\text{IR}}(t)$ interacts with the system, setting up first-order polarization (Figure 3)

$$P^{(1)}(t) = \int_{-\infty}^{+\infty} dt' E_{\text{IR}}(t-t') S(t') \quad (5)$$

This polarization persists after the IR pulse is over and oscillates at the eigenfrequencies of the system, decaying according to the total dephasing rate. $P^{(1)}(t)$ is upconverted into the 2nd-order polarization $P^{(2)}(t, \tau)$ by the time-delayed visible field $E_{\text{vis}}(t-\tau)$. Because the system's response to the nonresonant visible field is instantaneous, the second convolution is replaced by a product,

$$P^{(2)}(t, \tau) \propto E_{\text{vis}}(t-\tau) P^{(1)}(t) \quad (6)$$

The component of this second-order polarization oscillating at the IR + visible sum frequency radiates the SFG signal in the phase-matched direction. This emission is collected and time-integrated by the CCD detector resulting in the SFG–FID signal as a function of the time delay τ between IR and visible pulses:

$$I_{\text{SFG-FID}}(\tau) \propto \int_{-\infty}^{\infty} dt |P^{(2)}(t, \tau)|^2 \quad (7)$$

(Here we focus solely on the time- or frequency-dependence of the signals. We omit all other factors such as Fresnel coefficients, assuming that they are the same for all vibrational modes.) In our calculations, we approximate the field envelopes of the visible and IR pulses $E_{\text{IR}}(t)$ and $E_{\text{vis}}(t)$ as Gaussians with parameters determined from the autocorrelation and cross-correlation measurements (Figure 3) as described in the Experimental section. We then perform integrations per eqs 3–7 to compute the SFG–FID signals.

Unlike the “true” FID measurement (e.g., in NMR), SFG–FID does not record oscillations at the carrier frequency (in our case, vibrational frequency) because the surface-selective detection scheme requires up-conversion by the visible pulse.⁴⁸ Rather, the envelope of the oscillating surface polarization is measured.

In the frequency-domain, the broad-band SFG spectra are given by

$$I_{\text{SFG}}(\omega_{\text{SFG}}) \propto \left| \int_{-\infty}^{\infty} d\omega_{\text{IR}} E_{\text{vis}}(\omega_{\text{SFG}} - \omega_{\text{IR}}) [E_{\text{IR}}(\omega_{\text{IR}}) G(\omega_{\text{IR}})] \right|^2 \quad (8)$$

The term in square brackets describes spectrum of the first-order polarization $P^{(1)}(\omega_{\text{IR}})$ resulting from interaction of the IR field $E_{\text{IR}}(\omega_{\text{IR}})$ with the system's response function $G(\omega_{\text{IR}})$. The convolution integral represents up-conversion of $P^{(1)}(\omega_{\text{IR}})$ by the visible field $E_{\text{vis}}(\omega_{\text{vis}})$, resulting in SFG signal at frequency $\omega_{\text{SFG}} = \omega_{\text{vis}} + \omega_{\text{IR}}$. Spectra of the visible and IR pulses are measured independently (Experimental section, Figure 2) and approximated by Gaussian functions.

Instead of the time-consuming numerical fitting of the frequency-domain SFG spectra using the Voigt profile resulting from Gaussian–Lorentzian convolution in eq 8, we fit to a set of coherently added Lorentzians,

$$I_{\text{SFG}}(\omega_{\text{IR}} + \omega_{\text{vis}}^0) \propto \left| A_{\text{NR}} e^{i\varphi_{\text{NR}}} + \sum_i \frac{B_i \Gamma_i'}{\omega_{\text{IR}} - \omega_i + i\Gamma_i'} \right|^2 \exp \left[-\frac{(\omega_{\text{IR}} - \omega_{\text{IR}}^0)^2}{\Delta_{\text{IR}}^2} \right] \quad (9)$$

where ω_{IR}^0 and ω_{vis}^0 are central frequencies of the IR and visible pulse spectra, and the last term provides correction for the (independently measured) intensity spectrum of the IR pulse (we note that it is significantly broader, $\text{fwhm} \approx 300 \text{ cm}^{-1}$, than the region of the vibrational resonances, 2850–2950 cm^{-1}). The visible pulse spectral width was then deconvoluted from Γ_i' as described in the Results section to recover true Γ_i values.

5. Discussion

The time-domain SFG–FID and frequency-domain SFG spectral data were fitted simultaneously for each sample, using the computational procedure described above. The fitting parameters are sets of $(B_i, \omega_i, \Gamma_i)$ for each of the transitions, plus the nonresonant term $A_{\text{NR}} e^{i\varphi_{\text{NR}}}$. The resulting best simultaneous fits are shown in Figures 4–7 and the parameters are collected in Table 1. Assignment of the vibrational modes was done in accordance with the frequencies for long-chain alkanes³⁸ and similar surface monolayers reported in the literature.^{39,41,43,44} All amplitudes (of both resonant and nonresonant terms) have been normalized to the B value for the ν^+ (CH_3 SS) mode of sample 1.

For the well-ordered films transferred at high pressure (sample 1, 30 mN/m, LS phase and Sample 2, 15 mN/m, O_v mesophase), we find that two transitions, r^+ (symmetric stretch of the terminal methyl) and r^+_{FR} (Fermi resonance of r^+ with the bend overtone), are nearly sufficient for adequate description of both frequency- and time-domain data (Figures 4, 5).

The unified model described above shows how certain features of the frequency-domain spectra relate to the features of the time-domain free induction decay. For example, the period of the quantum beat between two modes (~ 540 fs) is the inverse difference frequency ($\Delta\nu \approx 60$ cm^{-1}); the overall decay time of the beat is related to the inverse line width Γ^{-1} ; and the modulation depth of the FID quantum beat pattern reflects the amplitude ratio of the two modes: for $\eta = B(r^+_{FR})/B(r^+) \approx 1$, one would expect nearly 100% modulation (e.g., in samples 1 and 2, Figures 4b, 5b), while for other ratios the FID beats do not reach zero, as in Figure 6b for Sample 3 ($\eta = 0.5$).

The amplitude ratio η could, in principle, be used to deduce orientation of the $-\text{CH}_3$ moiety. This, however, requires the precise knowledge of the molecular hyperpolarizability tensors $\beta_{abc}^{(2)}$ in the molecular frame (a,b,c), for both r^+ and r^+_{FR} modes. While the first is known reasonably well due to the symmetry of the r^+ mode,^{40,43,49} the second is not readily available. We can point out, however, that the varying amplitude ratio η found for samples 1–4 implies that (1) the average orientation of the terminal methyl group is different in different LB phases and mesophases and (2) the hyperpolarizability tensors for r^+ and r^+_{FR} modes are indeed different, which dismisses the common notion that, since most of the Fermi resonance transition intensity is borrowed from the symmetric stretch mode, $\beta_{abc}^{(2)}(r^+_{FR})$ should have the same symmetry as $\beta_{abc}^{(2)}(r^+)$.⁴⁹

In addition to the two main r^+ and r^+_{FR} transitions, a weak r^- mode (antisymmetric stretch of the terminal methyl) at 2956 ± 5 cm^{-1} (large frequency uncertainty due to small amplitude) is manifested in the frequency-domain spectra as a slight asymmetry of the r^+_{FR} line shape showing sharper decrease on the blue side. For the SSP polarization combination used in our measurement (SFG–S, visible–S, IR–P), the r^- mode is found to have negative amplitude relative to the r^+ and r^+_{FR} modes. As first noted by Wolfrum and Laubereau,⁴³ this is a result of orientational averaging (see eq 10 below) of the molecular hyperpolarizability tensors $\beta_{abc}^{(2)}$, which are different for the antisymmetric and symmetric modes.

The negative amplitude of the r^- mode increases from sample 1 (ordered LS phase) to samples 3 and 4 (less-ordered LC phase). Note that this is not evident from the frequency-domain SFG spectra alone (Figures 6a, 7a). Although a thorough study of molecular orientation is outside of the scope of this paper, a qualitative analysis of the obtained transition amplitudes using the model developed by Wolfrum and Laubereau⁴³ shows that the increasing negative amplitude of the antisymmetric stretch r^- relative to r^+ (Table 1) implies increasing angle θ of the terminal methyl group with respect to surface normal (Figure 8), viz.

$$\frac{B_{\text{SSP}}(r^-)}{B_{\text{SSP}}(r^+)} = -\frac{\kappa}{2} \frac{\langle \cos \theta \rangle - \langle \cos^3 \theta \rangle}{(\gamma + 1)\langle \cos \theta \rangle - (\gamma - 1)\langle \cos^3 \theta \rangle} \quad (10)$$

where $\kappa = \beta_{caa}^{(2)}(r^-)/\beta_{ccc}^{(2)}(r^+)$ and $\gamma = \beta_{aac}^{(2)}(r^+)/\beta_{ccc}^{(2)}(r^+)$. This, in turn, implies increasing tilt of the alkyl chain Θ with decreasing surface pressure (for random twist angle of the alkyl backbone planes reported in the literature,^{28,30} $\langle \theta \rangle = \Theta$, Figure 8). If we assume an average chain tilt angle for sample 1 (based on the

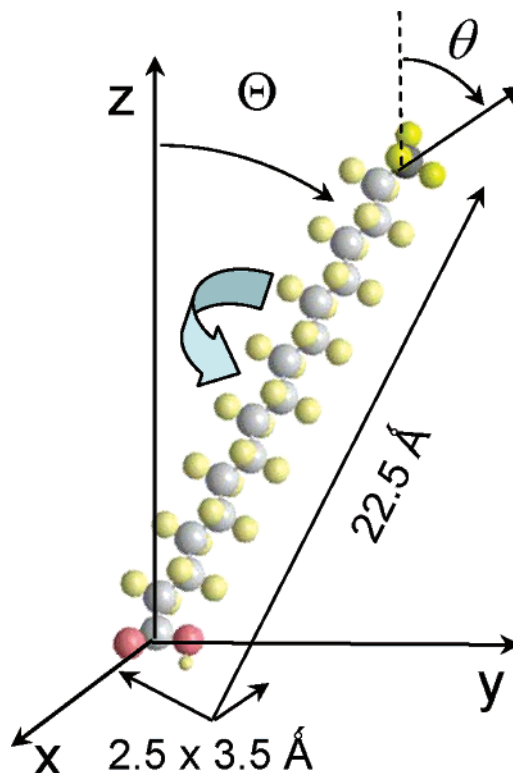


Figure 8. Molecular orientation angles for HDA on a plane substrate surface (x – y plane). θ is the tilt angle of the C_3 axis of the terminal methyl group with respect to surface normal (z -axis). Θ is the average tilt angle of the carbon chain. Random orientation of the alkyl backbone planes (indicated by ribbon arrow) is assumed for the 2D monolayer phases studied in this work (ref 28).

X-ray studies of similar monolayers, nearly vertical chains are expected, $\Theta = 3$ – 12°),²⁸ we can estimate a chain tilt of $\Theta \approx 7$ – 20° for sample 3 and $\Theta \approx 9$ – 25° for sample 4. The difference in the tilt angle between samples 2 and 3, transferred at nominally the same surface pressure, may be indicative of the two different mesophases: O_v with next-to-nearest neighbor (NNN) tilt for sample 2 vs L_{2d} with larger tilt toward nearest neighbor (NN) for sample 3, in qualitative agreement with the X-ray results.³⁰ We note that determining molecular orientation from the relative amplitudes of two different modes has certain advantages over the usually performed measurements of different polarization combinations. For example, since both modes are measured with the same polarization combination, the Fresnel factors in eq 10 cancel out, which eliminates the uncertainty due to unknown refractive index of the surface layer.⁴⁰

In the frequency-domain SFG spectra of sample 4, transferred at surface pressure 5 mN/m, two main transitions are accompanied by weak shoulders (Figure 7a). The difference between this sample and the more ordered monolayers transferred at higher surface pressures is more apparent in the time-domain SFG–FID measurement (Figure 7b), which shows a very short-lived vibrational coherence.

Figure 7a demonstrates the difficulty of separating the overlapping spectral components from the frequency-domain spectra: the calculated best fit SFG spectra using two vs five transitions are very similar. However, two vibrational modes in eqs 1–4 are not sufficient to obtain even a marginally satisfactory simultaneous fit of both the frequency- and time-domain data. In fact, we find that a minimum of five modes are necessary. This is an example where time-domain SFG–FID data can significantly amplify the sensitivity in determining

the model fitting parameters. Figures 7a,b show the fits using five vs two transitions, demonstrating that it is possible to obtain a good fit of the SFG spectra, yet the SFG–FID clearly requires introduction of additional resonances. The fast decay of the vibrational coherence in this case results from interference of several vibrational modes at different frequencies, rather than from broadening of two main transitions.

The need to introduce the CH₂ stretch modes in sample 4 may be indicative of the increased amount of gauche defects in this less-ordered monolayer, due to increased conformational freedom provided by a larger surface area per molecule. We point out that the LC phase monolayers are composed of a heterogeneous mixture of mesophase domains. The average size of the domains (from BAM measurements)³² is of the order of 10–100 μm , which is somewhat smaller than the beam size in the present measurement ($\sim 250 \mu\text{m}$). Our results therefore likely represent an average over the heterogeneous mesophase composition at a given pressure.

To fit sample 4 data, we also need to assume the presence of a strong nonresonant term. This may arise from the OH-stretch mode of water molecules trapped in the hydrophilic region of the LB monolayer. Hydrogen-bonding may frequency-shift the ν_{OH} band, centered at 3200–3500 cm^{-1} , by hundreds of wavenumbers, resulting in spectral wings overlapping the CH-stretch modes.

The disagreement between the model calculation and experimental SFG–FID curves at early times (of the order of instrument response), e.g., in Figures 6b and 7b, is most likely due to inadequate description of the residual chirp in the IR and visible pulses.

Simultaneous fitting of the frequency- and time-domain data enabled by the unified model demonstrates the utility of this combined spectroscopic approach for samples with complex congested spectra. The frequency- vs time-domain measurements are sensitive to different aspects of the molecular response function: while frequency-domain spectroscopy is best suited for well-resolved lines, time-domain FID proves more sensitive to broad and overlapping transitions which results in fast decay of coherence. At the same time, determination of the true line width for spectrally narrow transitions is also more accurately performed in the time-domain. While frequency-domain spectral resolution usually comes at a price of reduced signal levels, time domain measurement of a spectrally narrow, i.e., long-lived vibrational coherence simply entails scanning over a longer IR-visible delay, with no practical difficulties out to nanoseconds (1 ns translates into 0.03 cm^{-1} spectral resolution). Insets in Figures 4b–6b demonstrate the superior signal-to-noise ratio for the time-domain signals vs frequency-resolved SFG spectra, allowing to follow the decay of the vibrational coherences over almost 3 decades of the SFG–FID signal. Making use of the information redundancy of these Fourier transform connected measurements thus may enable a more accurate determination of the molecular response function parameters.

The difference in the spectra and FID curves of samples 2 and 3 demonstrates the potential of the combined frequency- and time-domain SFG for distinguishing different phases and even mesophases of LB monolayers. Possible applications of this approach include comparative studies of LB monolayers before and after transfer, which will allow characterization of the transfer process and its effect on the molecular structure of the film. The noninvasive nature of the SFG techniques makes them uniquely suited for such studies.

The observed line widths Γ_i , from 4 to 25 cm^{-1} , correspond to the vibrational dephasing times, $\tau_i = 1/\Gamma_i$, of the order of

1–5 ps. Being essentially a linear spectroscopic technique (one resonant interaction with the light field), the time-domain SFG–FID measures the total dephasing time, and therefore does not allow to experimentally dissect the broadening mechanisms. Although the observed time scales are of the same order of magnitude as the vibrational population lifetimes in condensed phases (usually of the order of a few ps), the static disorder cannot be eliminated as the contributing factor to the observed dephasing rates. Higher order nonlinear surface spectroscopies, such as 4th-order techniques of pump–SFG probe¹⁶ and SFG photon echo,^{11,48} are needed for more detailed insight into the molecular dynamics at surfaces. The future development of these techniques will undoubtedly prove essential for deciphering the dynamics in complex systems characterized by the mode coupling, congested spectra, and fast FID decay, whose spectra and dynamics cannot be adequately interpreted based on the linear techniques.

6. Conclusions

Coherent quantum beats in time-domain SFG–FID complement frequency-domain SFG spectroscopy to make a sensitive tool for characterizing molecular organization in monolayer films. Redundant information in the time- and frequency-domain, utilized via simultaneous fitting of the SFG spectra and SFG–FID curves within the unified model, allows more accurate determination of the parameters of the response function. The combined measurements may therefore prove advantageous over purely frequency- or time-domain techniques for samples with complex congested spectra and/or broad and overlapping transitions.

Our measurements indicate different molecular orientation and conformation of heptadecanoic acid Langmuir–Blodgett monolayers in different two-dimensional phases and mesophases. Highly ordered films transferred at high surface pressure (superliquid phase), with nearly vertical alkyl chains in all-trans conformation, exhibit two dominant narrow vibrational modes in the frequency domain SFG, CH₃ symmetric stretch (2875 cm^{-1}) and bend overtone enhanced by Fermi resonance (2935 cm^{-1}), and a long-lived coherent quantum beat in the time-domain SFG–FID at the difference frequency (~ 540 fs period). Monolayers in the less-ordered liquid condensed phase and its mesophases, transferred at lower surface pressures, show more congested SFG spectra with additional transitions appearing as weak shoulders (CH₃ asymmetric stretch and CH₂ modes), which also alter the time-domain quantum beats and result in faster decay of the vibrational coherence. Simultaneous fitting of the frequency- and time-domain SFG data by the presented model yields parameters of the molecular response function (transition frequencies, widths, and amplitudes), providing insight into molecular orientation, conformation, and onset of disorder in the Langmuir–Blodgett monolayers.

Acknowledgment. The authors gratefully acknowledge the start-up funds from Wayne State University and the Wayne State Research Fellowship. Acknowledgment is made to the donors of the American Chemical Society Petroleum Research Fund for partial support of this research under the ACS-PRF grant #40868-G6. We thank Prof. Sandro da Rocha and Ms. Shang-Chieh Lin of the Wayne State Chemical Engineering Department for the use of the Langmuir–Blodgett trough and their help in sample preparation. Assistance of Mr. Tibebe Lemma in the initial stages of this project is also acknowledged.

References and Notes

- (1) *Ultrafast Infrared and Raman Spectroscopy*; Fayer, M. D., Ed.; Marcel Dekker: New York, 2001; Vol. 26.

- (2) Zanni, M. T.; Hochstrasser, R. M. *Curr. Opin. Struct. Biol.* **2001**, *11*, 516.
- (3) Demirdoven, N.; Khalil, M.; Tokmakoff, A. *Phys. Rev. Lett.* **2002**, *89*, Art. No. 237401.
- (4) Asplund, M. C.; Lim, M.; Hochstrasser, R. M. *Chem. Phys. Lett.* **2000**, *323*, 269.
- (5) Ge, N. H.; Hochstrasser, R. M. *PhysChemComm* **2002**, *3*, 17.
- (6) Rector, K. D.; Fayer, M. D. *Int. Rev. Phys. Chem.* **1998**, *17*, 261.
- (7) Asbury, J. B.; Steinel, T.; Stromberg, C.; Gaffney, K. J.; Piletic, I. R.; Goun, A.; Fayer, M. D. *Chem. Phys. Lett.* **2003**, *374*, 362.
- (8) Blank, D. A.; Kaufman, L. J.; Fleming, G. R. *J. Chem. Phys.* **2000**, *113*, 771.
- (9) Khalil, M.; Demirdoven, N.; Tokmakoff, A. *J. Phys. Chem. A* **2003**, *107*, 5258.
- (10) Cho, M. *PhysChemComm* **2002**, *5*, 40.
- (11) Guyot-Sionnest, P. *Phys. Rev. Lett.* **1991**, *66*, 1489.
- (12) Owrutsky, J. C.; Culver, J. P.; Li, M.; Kim, Y. R.; Sarisky, M. J.; Yeganeh, M. S.; Yodh, A. G.; Hochstrasser, R. M. *J. Chem. Phys.* **1992**, *97*, 4421.
- (13) Culver, J. P.; Li, M.; Jahn, L. G.; Hochstrasser, R. M.; Yodh, A. G. *Chem. Phys. Lett.* **1993**, *214*, 431.
- (14) Culver, J. P.; Li, M.; Hochstrasser, R. M.; Yodh, A. G. *Surf. Sci.* **1996**, *368*, 9.
- (15) Bonn, M.; Hess, C.; Wolf, M. *J. Chem. Phys.* **2001**, *115*, 7725.
- (16) Hess, C.; Wolf, M.; Roke, S.; Bonn, M. *Surf. Sci.* **2002**, *502*, 304.
- (17) Roke, S.; Kley, A. W.; Bonn, M. *J. Phys. Chem. A* **2001**, *105*, 1683.
- (18) Star, D.; Kikteva, T.; Leach, G. W. *J. Chem. Phys.* **1999**, *111*, 14.
- (19) Roke, S.; Kley, A. W.; Bonn, M. *Chem. Phys. Lett.* **2003**, *370*, 227.
- (20) Katz, H. E.; Bao, Z. N.; Gilat, S. L. *Acc. Chem. Res.* **2001**, *34*, 359.
- (21) Paloheimo, J.; Kuivalainen, P.; Stubb, H.; Vuorimaa, E.; Ylilahti, P. *Appl. Phys. Lett.* **1990**, *56*, 1157.
- (22) Xu, G. F.; Bao, Z. A.; Groves, J. T. *Langmuir* **2000**, *16*, 1834.
- (23) Ding, H. M.; Ram, M. K.; Nicolini, C. J. *Mater. Chem.* **2002**, *12*, 3585.
- (24) Endo, T.; Takeoka, Y.; Rikukawa, M.; Sanui, K. *Synth. Met.* **2003**, *135*, 333.
- (25) Wang, G. M.; Swensen, J.; Moses, D.; Heeger, A. J. *J. Appl. Phys.* **2003**, *93*, 6137.
- (26) Bune, A.; Fridkin, V.; Ducharme, S.; Blinov, L.; Palto, S.; Sorokin, A.; Yudin, S.; Zlatkin, A. *Nature* **1998**, *391*, 874.
- (27) Reece, T. J.; Ducharme, S.; Sorokin, A. V.; Poulsen, M. *Appl. Phys. Lett.* **2003**, *82*, 142.
- (28) Bohanon, T. M.; Lin, B.; Shih, M. C.; Ice, G. E.; Dutta, P. *Phys. Rev. B* **1990**, *41*, 4846.
- (29) Gaines, G. L., Jr. *Insoluble Monolayers at Liquid-Gas Interfaces*; Interscience Publishers: J. Wiley & Sons: New York, 1966.
- (30) Kaganer, V. M.; Peterson, I. R.; Kenn, R. M.; Shih, M. C.; Durbin, M.; Dutta, P. *J. Chem. Phys.* **1995**, *102*, 9412.
- (31) Ramos, S.; Castillo, R. *J. Chem. Phys.* **1999**, *110*, 7021.
- (32) Riviere, S.; Henon, S.; Meunier, J.; Schwartz, D.; Tsao, M.; Knobler, C. *J. Chem. Phys.* **1994**, *101*, 10045.
- (33) Halperin, K.; Ketterson, J. B.; Dutta, P. *Langmuir* **1989**, *5*, 161.
- (34) Richter, L. T.; Petralli-Mallow, T. P.; Stephenson, J. C. *Opt. Lett.* **1998**, *23*, 1594.
- (35) Hommel, E. L.; Ma, G.; Allen, H. C. *Anal. Sci.* **2001**, *17*, 1325.
- (36) Bonn, M.; Kley, A. W.; Kroes, G. J. *Surf. Sci.* **2002**, *500*, 475.
- (37) Bordenyuk, A. N.; Benderskii, A. V. *J. Chem. Phys.* **2005**, *122*, 134713.
- (38) MacPhail, R. A.; Straws, H. L.; Snyder, R. G.; Elliger, C. A. *J. Phys. Chem.* **1984**, *88*, 334.
- (39) Guyot-Sionnest, P.; Hunt, J. H.; Shen, Y. R. *Phys. Rev. Lett.* **1987**, *59*, 1597.
- (40) Zhuang, X.; Miranda, P. B.; Kim, D.; Shen, Y. R. *Phys. Rev. B* **1999**, *59*, 12632.
- (41) Gragson, D. E.; McCarty, B. M.; Richmond, G. L. *J. Am. Chem. Soc.* **1997**, *119*, 6144.
- (42) Akamatsu, N.; Domen, K.; Hirose, C. *J. Phys. Chem.* **1993**, *97*, 10070.
- (43) Wolfrum, K.; Laubereau, A. *Chem. Phys. Lett.* **1994**, *228*, 83.
- (44) Ward, R. N.; Duffy, D. C.; Davies, P. B.; Bain, C. D. *J. Phys. Chem.* **1994**, *98*, 8536.
- (45) Bloembergen, N. *Nonlinear Optics*; Benjamin: New York, 1965.
- (46) Levenson, M. D. *Introduction to Nonlinear Laser Spectroscopy*; Academic Press: New York, 1982.
- (47) Mukamel, S. *Principles of Nonlinear Optical Spectroscopy*; Oxford University Press: New York, 1995.
- (48) Ueba, H. *Prog. Surf. Sci.* **1997**, *55*, 115.
- (49) Hirose, C.; Akamatsu, N.; Domen, K. *J. Chem. Phys.* **1992**, *96*, 997.